

Rydberg Vision via frugal Quantum Image Fingerprinting

Vikrant Sharma^{1,*} and Neel Kanth Kundu^{2,†}

¹*Electrical Engineering Department, Dayalbagh Educational Institute, Agra, India*

²*Centre for Applied Research in Electronics (CARE),
Indian Institute of Technology Delhi, New Delhi, India*

(Dated: March 11, 2026)

Gate-based quantum image processing is constrained by qubit scarcity and the high overhead of quantum state preparation, limiting its applicability to realistic geometric data. We introduce a quantum-native framework for image matching on neutral-atom analog quantum computers that advances our earlier Sparse-Dots Representation (SDR) approach. A classical pre-processing pipeline—Sobel edge extraction followed by the Ramer–Douglas–Peucker (RDP) algorithm—converts an input image into a geometrically faithful Sparse-Dots point cloud of substantially fewer atoms. This atom layout is virtually embedded into the programmable tweezer array of QuEra’s Aquila device via its Bloqade SDK, where the image geometry is encoded physically in the distance-dependent van der Waals interaction term of the Rydberg Hamiltonian. After time-evolution, we extract the many-body fingerprint of each image using two observables—the Pearson-normalized two-site correlation matrix which encodes the blockade-induced correlation structure of the quantum state, and the two-dimensional static structure factor evaluated on a fixed wavevector grid, yielding a fingerprint vector of constant length regardless of atom count. In Stage 1, image matching is performed by cosine similarity on the fingerprint vectors, a scale-invariant metric appropriate for Fourier-domain descriptors. In Stage 2, this approach is extended to quantum reservoir computing (QRC) to enable machine learning via dramatically reduced training data and training cycles, as a preliminary proof-of-concept. Simulations using the Bloqade software stack confirm successful matching of industrial objects, often with fewer than 24 atoms. To our knowledge, this constitutes the first application of the static structure factor—a condensed-matter quantum observable—as an image retrieval descriptor in an analog quantum computing context.

I. INTRODUCTION

Human visual recognition is remarkably energy and data efficient. In familiar environments, individuals are often identified without reliance on full-frontal facial information, instead using coarse geometric cues such as body build, posture, or partial views. This process is robust to occlusion and illustrates that accurate recognition does not require complete or high-resolution visual data.

Motivated by this observation, we explore whether analogous principles can be exploited for quantum-native processing of geometric data on current quantum hardware. Rather than encoding full pixel-level information, we focus on sparse geometric representations that preserve structural content while discarding redundant detail. Such representations naturally reduce quantum resource requirements, making them well suited for the noisy intermediate-scale quantum (NISQ) regime. By contrast, existing approaches to quantum image processing predominantly rely on digital encodings of pixel data into quantum states, which incur substantial state-preparation overhead and scale poorly under current qubit constraints [1].

In this work, we introduce a quantum-native framework for encoding and processing sparse geometric data

directly into interacting many-body quantum systems. Instead of mapping images onto digital basis states, geometric information is embedded through the sparse spatial arrangement of neutral atoms, allowing native interatomic interactions to encode structural relationships. Under global Rydberg driving, these atomic configurations evolve into correlated quantum states whose connected density correlations reflect the underlying geometry. We show that these emergent many-body correlations form compact and experimentally accessible signatures of sparse visual structures. By comparing correlation signatures across different inputs, robust matching can be achieved using fixed Hamiltonian evolution and projective measurements alone, without explicit digital quantum circuits or classical feature extraction. **The Hamiltonian itself is the Interferometer.** These results establish many-body correlations as a natural similarity metric for geometric data on analog quantum devices and highlight the potential of neutral-atom platforms as resource-efficient, quantum-native alternatives to classical image processing pipelines.

A. Quantum Image Processing

Quantum image processing (QImP) [2] exploits quantum mechanical properties—superposition, entanglement, and interference—to represent and manipulate images. Through massive parallel state evolution, QImP can provide advantages over classical image processing for selected operations. Quantum image representation

* vikrant@dei.ac.in

† neelkanth@iitd.ac.in

(QImR) is the foundational step: it determines which processing tasks are feasible and at what cost, as it governs both the nature of image encoding and the realizable processing tasks. Edge extraction is a fundamental operation within QImP. With the rapid growth of high-resolution and high-throughput image data, large-scale real-time classical edge processing increasingly faces challenges in energy consumption, latency, and system-level scalability—thereby motivating quantum and hybrid processing strategies. Analog quantum platforms offer an alternative paradigm in which physical interactions and interference directly generate expressive similarity measures, without explicit feature construction or optimization loops. Emergent many-body correlations thus provide a natural substrate for quantum-native pattern recognition, and suggest a pathway toward reservoir-style learning on near-term neutral-atom hardware.

B. Why Quantum Machine Learning for Image Processing?

Machine learning (ML) encompasses computational methods for extracting patterns from data, including classification, regression, clustering, and related tasks. Classical ML methods, particularly kernel-based classifiers, often face fundamental scalability limitations when applied to data with highly nonlinear and high-dimensional structure, as the explicit construction and evaluation of complex feature spaces rapidly becomes computationally prohibitive. Quantum ML (QML) [3–5] offers a principled alternative by exploiting the exponentially large Hilbert space of a quantum system as a natural feature space, enabling efficient realization of rich nonlinear kernel functions via quantum state preparation and entangling operations [5]. As demonstrated by Havlíček et al. [4], quantum-enhanced feature maps can induce class separability that is difficult or infeasible to replicate using classical kernels of comparable computational cost. Certain subroutines in AI/ML—linear algebra, kernel methods, sampling, and combinatorial optimisation—admit quantum algorithms with provable speedups, motivating the study of quantum-native learning models that leverage interference and entanglement to construct expressive similarity measures. Early evidence suggests that quantum annealing and analog quantum computers can be integrated into quantum-classical AI workflows, potentially enhancing model efficiency and reducing energy consumption [6, 7].

a. Energy efficiency. QuEra’s *Aquila* [8], a neutral-atom quantum device with up to 256 programmable atom qubits, typically operates on less than 7 kW for the full system—according to industry estimates, less than 0.05% of the power required by a classical AI supercomputer [9]. While control electronics, vacuum systems, and laser-stabilization infrastructure contribute a broadly fixed overhead that does not vanish at zero atoms, the qubit-related power costs (laser drive and atom trapping) do

not scale strongly with atom count in neutral-atom architectures. This is in marked contrast to classical computing, where active transistor count drives energy consumption near-linearly with the number of processing elements, making neutral-atom devices particularly attractive for qubit-count scale-up. For comparison, gate-based quantum computers from IBM, Rigetti and Google consume approximately 10–25 kW [9].

b. Native combinatorial optimization. The device provides hardware-native heuristic solutions to Maximum Independent Set (MIS) problems using the Rydberg blockade [10]—a task for which even heuristic classical solvers (simulated annealing, greedy algorithms) can require hours to days on graphs with hundreds of nodes. MIS is directly relevant to ML tasks including feature selection, graph-based clustering, and resource allocation in networks.

c. Quantum reservoir computing. Quantum reservoir computing (QRC) on such hardware requires as few as ~ 300 training samples, avoids gradient descent entirely, and therefore does not suffer from the vanishing gradient problem [6, 11]. Once an image is encoded in the quantum device, the many-body Rydberg system acts as a fixed nonlinear feature map, with learning performed entirely in classical post-processing—conserving both energy and computational resources relative to deep-learning training pipelines.

C. Motivation for Quantum-Native Fingerprinting

A fundamental limitation of our earlier SDR work [12] was that image *matching* was performed by a classical Chamfer distance [13] computed on the post-simulation Rydberg density plots—a classical geometric metric applied to a quantum output. This approach failed to exploit the rich many-body quantum correlations generated by the Rydberg Hamiltonian, and discarded the most quantum information the device produced.

The present work addresses this gap by extracting a fully quantum fingerprint directly from the evolved quantum state: the Pearson-normalized connected correlation matrix and the derived 2D static structure factor. The structure factor is a well-established condensed-matter observable [14] routinely used to characterize quantum phases in Rydberg arrays; here we apply it as an image descriptor for the first time. Matching is then performed by cosine similarity on the structure-factor fingerprint—a scale-invariant metric appropriate for Fourier-domain representations.

D. Cartographic Generalization and RDP

Cartographic generalization (CG) [15–17] denotes the systematic simplification of spatial data while preserving its essential geometric structure. Traditionally developed within cartography to enable the depiction of geo-

graphic entities—roads, rivers, coastlines—across varying map scales, CG encompasses line simplification, smoothing, aggregation, and displacement techniques. Its computational efficiency, geometric interpretability, and parameter-based control over the degree of simplification make it indispensable not only in cartography but also in computer vision, robotics, and image-based shape abstraction.

The most influential line simplification technique in CG is the Ramer–Douglas–Peucker (RDP) algorithm [15, 16], independently proposed by Urs Ramer (1972) and later by Douglas and Peucker (1973). RDP operates on the principle of recursive distance thresholding. Given a polyline $\{P_i\}_{i=1}^n$, the algorithm computes the perpendicular distance of each intermediate point P_k from the baseline $\overline{P_1P_n}$:

$$d(P_k, \overline{P_1P_n}) = \frac{\|(P_n - P_1) \times (P_1 - P_k)\|}{\|P_n - P_1\|}. \quad (1)$$

This perpendicular distance is the decision metric of RDP. A point P_k is recursively retained if and only if

$$\max_{k \in \{2, \dots, n-1\}}, d(P_k, \overline{P_1P_n}) > \varepsilon, \quad (2)$$

where ε is the user-specified tolerance parameter; points with distance less than ε are discarded. By adjusting ε , users balance geometric precision against data compactness. In our pipeline, ε is adaptively raised until the retained point count satisfies the hardware atom-number cap, guaranteeing a structurally faithful yet qubit-frugal atom array.

II. RELATED WORK

Most prior quantum image processing research operates in the digital paradigm, employing representations such as FRQI, QPIE, and NEQR whose qubit requirements scale with image resolution [1]. Quantum circuit simulations of low-resolution images emphasize exponential speedups but remain impractical for real-world image sizes.

Yao et al. [2] demonstrated NMR-based quantum edge detection on a 4×4 image using QPIE encoding and Quantum Hadamard Edge Detection (QHED), achieving $\mathcal{O}(1)$ boundary detection. Despite the elegance of this result, qubit scarcity and NMR noise present severe obstacles to scaling. Cavalieri and Maio [18] improved QHED using central finite differences, but validated results through classical simulation only; decoherence and gate noise degrade the results severely on physical gate-based hardware.

Kornjača et al. [6] introduced quantum reservoir computing on QuEra’s Aquila by encoding downscaled tomato-leaf images via vertical inter-atom distances in a 9×9 atom grid, yielding 72-pixel resolution with 81 qubits. This scheme scales qubit count linearly with pixel

count: 108 qubits for 96 pixels. Such resolutions are insufficient for most real-world applications.

Lu et al. [19] proposed hybrid digital-analog Rydberg learning on Quantum Phase (QPL) and MNIST. Their approach requires trainable parameters, a classical optimiser, and labelled data—it is a supervised classifier, not an unsupervised retrieval system.

In contrast, our Sparse-Dots Representation (SDR) overcomes all these limitations. The qubit count is determined solely by geometric complexity—governed by the application-specific tolerance parameter and available hardware resources—rather than by pixel resolution, making SDR directly compatible with Aquila’s global analog control. To our knowledge, SDR is the only analog quantum image representation with this property, enabling compact encoding of real-world image sizes and high-fidelity simulation of large, geometrically complex structures—a flexibility unavailable to techniques like FRQI [1], NEQR [20] or QPIE [2]. The present work further advances SDR by replacing the classical Chamfer-distance matching [12] with a fully quantum-native fingerprint, based on many-body correlations and the 2-D static structure factor.

Table I summarizes the comparison. The key differentiator of this work is: a variable-length fingerprint enabling direct comparison across images with different atom counts, with the first use of the static structure factor as an image descriptor.

III. METHOD: SPARSE-DOTS REPRESENTATION AND QUANTUM FINGERPRINTING

A. Rydberg Hamiltonian

The dynamics of the neutral-atom array on Aquila are governed by the time-dependent Rydberg Hamiltonian [8]:

$$H(t) = \frac{\Omega(t)}{2} \sum_j (|g_j\rangle\langle r_j| + |r_j\rangle\langle g_j|) + \sum_{j < k} V_{jk} \hat{n}_j \hat{n}_k - \sum_j [\Delta_g(t) + \alpha_j \Delta_l(t)] \hat{n}_j, \quad (3)$$

where $\Omega(t)$ is the global Rabi frequency, $\hat{n}_j = |r_j\rangle\langle r_j|$ is the Rydberg number operator at site j , $\Delta_g(t)$ is the global detuning, $\Delta_l(t)$ is an optional local detuning scaled by the site factor α_j , and

$$V_{jk} = \frac{C_6}{|\mathbf{r}_j - \mathbf{r}_k|^6} \quad (4)$$

is the van der Waals blockade interaction. This r^{-6} dependence is the key mechanism: atoms placed according to an image’s geometric skeleton interact with strengths that precisely encode the pairwise distances of the image

TABLE I: Comparison of quantum image-processing methods and classical SIFT. Image dimension ($2^n \times 2^n$ pixels).

Method	Encoding	Observables	Task	Fingerprint dim
This work	Sobel + RDP sparse dots	$\tilde{C}_{ij}, S(\mathbf{k})$	Classification	Variable(72 std.)
Kornjača 2024 [6]	Atom-position/local-detuning	$\langle Z_j \rangle, \langle Z_j Z_k \rangle$	Time-series, Classification	Variable
Lu 2024 [19]	PCA product states	Single-qubit	Supervised MNIST, QPL	N/A
FRQI/QPIE/NEQR [1, 20]	Pixel-amplitude/basis-state	Amplitude/Basis-state	General QImP	4^n -scale
Classical SIFT	Keypoint descriptors	Local image gradients	Matching/retrieval	Variable(128 std.)

contour, embedding the image's shape into the many-body quantum state $|\psi(T)\rangle$. We follow the standard Bloqade/QuEra convention in which the drive term is written with an explicit factor of $\frac{1}{2}$, so that a resonant π -pulse satisfies $\Omega_{\max} t_\pi = \pi$.

B. Pipeline Overview

The full Stage 1 workflow (without QRC), illustrated in Fig. 1, consists of a classical pre-processing stage followed by quantum time-evolution and a quantum-native fingerprinting and matching stage.

C. Classical Pre-Processing: SDR Construction

a. Sobel edge extraction. The input image is converted to grayscale and convolved with the Sobel kernels S_x and S_y to yield gradients $G_x = S_x * I$ and $G_y = S_y * I$, whose magnitudes approximate $|\nabla I| \approx |G_x| + |G_y|$. Edge pixels are identified as those exceeding a threshold τ (typically 0.3-0.5 of the normalised magnitude).

b. Uniform pre-sampling. The set of edge pixels is uniformly sub-sampled with stride d (typically 50-90 pixels) to produce a tractable initial point cloud.

c. RDP with atom cap. The RDP algorithm is applied with tolerance ε . To guarantee that the resulting atom count $N \leq N_{\max}$ (typically 24, determined by the computational budget 2^N), ε is adaptively increased by a factor of 1.25 per iteration until the cap is satisfied. This eliminates both the duplicate-atom crash (which would produce $V_{jk} \rightarrow \infty$) and the non-geometric uniform-index subsampling of earlier structure-factor codes.

d. Physical scaling. Each retained (x, y) pixel coordinate is multiplied by the physical pixel size δ_μ (in $\mu\text{m}/\text{pixel}$) to produce the atom coordinates \mathbf{r}_j passed to Bloqade.

D. Quantum Encoding and Time Evolution

The N atom positions $\{\mathbf{r}_j\}$ are loaded into the programmable tweezer array. The quantum register is initialised in the all-ground state $|\psi(0)\rangle = |g\rangle^{\otimes N}$. The Rydberg Hamiltonian [Eq. (3)] is applied with a piecewise-

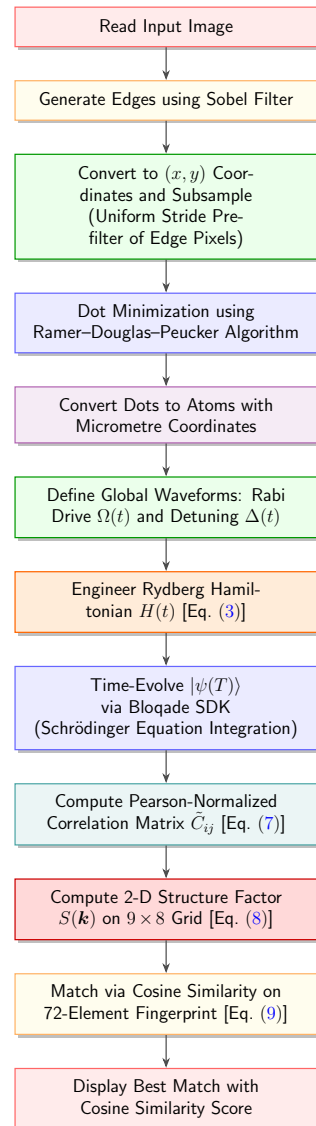


FIG. 1: Complete pipeline for quantum-native image matching (Stage 1). Upper eight blocks constitute the classical pre-processing and quantum encoding stage introduced in [12]. Lower four blocks constitute the new quantum fingerprinting and matching stage introduced in this work, replacing the classical Chamfer-distance matching used previously.

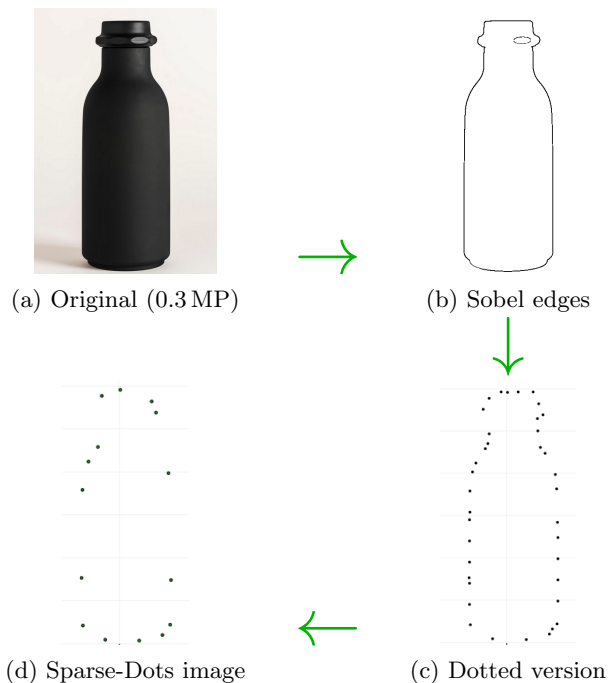


FIG. 2: Image pre-processing steps. (a) Original 0.3-megapixel image. (b) Sobel filter output. (c) Edge pixels replaced by equidistant dots. (d) Sparse-Dots image after RDP compression (typically $N = 10\text{--}20$ dots).

linear Rabi drive

$$\Omega(t) : 0 \xrightarrow{0.2 \mu\text{s}} \Omega_{\text{max}} \xrightarrow{0.6 \mu\text{s}[\text{plateau}]} \Omega_{\text{max}} \xrightarrow{0.2 \mu\text{s}} 0,$$

and a simultaneous three-segment detuning waveform

$$\Delta(t) : \begin{cases} -2\pi \times 12 \text{ MHz} & 0 \leq t \leq 0.2 \mu\text{s}, \\ \text{linear ramp to } +2\pi \times 10 \text{ MHz} & 0.2 < t < 0.8 \mu\text{s}, \\ +2\pi \times 10 \text{ MHz} & 0.8 \leq t \leq 1.0 \mu\text{s}, \end{cases}$$

over total evolution time $T = 1 \mu\text{s}$. The detuning sweep drives the system from a disordered regime toward a blockade-constrained many-body configuration determined by the image geometry.

IV. QUANTUM FINGERPRINTING: CORRELATIONS AND STRUCTURE FACTOR

This section presents the new contribution of this paper: the extraction of a fixed-length, quantum-native image fingerprint from the evolved state $|\psi(T)\rangle$. The quantum character of the protocol arises entirely from the many-body interference encoded in the connected correlators, which cannot be reconstructed from single-particle observables alone.

A. Exact Statevector Expectation Values

In the simulation, we work with the full statevector $|\psi\rangle \in \mathbb{C}^{2^N}$. The single-site Rydberg occupation and the two-site joint occupancy are computed exactly as

$$\langle \hat{n}_i \rangle = \sum_{k=0}^{2^N-1} |\psi_k|^2 n_i^{(k)}, \quad (5)$$

$$\langle \hat{n}_i \hat{n}_j \rangle = \sum_{k=0}^{2^N-1} |\psi_k|^2 n_i^{(k)} n_j^{(k)}, \quad (6)$$

where $n_i^{(k)} \in \{0, 1\}$ is the Rydberg occupation of atom i in basis state k . Bloqade/Yao uses LSB-first (little-endian) qubit ordering: qubit i occupies bit position $i-1$ of k , i.e. $n_i^{(k)} = (k \gg (i-1)) \& 1$. On hardware, $\langle \hat{n}_i \rangle$ is estimated from projective measurements (Rydberg density readout), and $\langle \hat{n}_i \hat{n}_j \rangle$ from shot-based joint excitation counts.

B. Pearson-Normalized Correlation Matrix

The raw connected two-site correlator is $C_{ij}^{\text{raw}} = \langle \hat{n}_i \hat{n}_j \rangle - \langle \hat{n}_i \rangle \langle \hat{n}_j \rangle$. Because \hat{n}_i is a projector ($\hat{n}_i^2 = \hat{n}_i$), its variance is exactly $\text{Var}(\hat{n}_i) = \langle \hat{n}_i \rangle (1 - \langle \hat{n}_i \rangle)$. The Pearson-normalized correlation is

$$\tilde{C}_{ij} = \frac{\langle \hat{n}_i \hat{n}_j \rangle - \langle \hat{n}_i \rangle \langle \hat{n}_j \rangle}{\sqrt{\text{Var}(\hat{n}_i) \cdot \text{Var}(\hat{n}_j) + \varepsilon_{\text{norm}}}}, \quad (7)$$

where $\varepsilon_{\text{norm}} = 10^{-8}$ prevents division by zero when a site has zero variance. By construction $\tilde{C}_{ij} \in [-1, +1]$, with $\tilde{C}_{ij} = -1$ indicating perfect blockade suppression, $\tilde{C}_{ij} = 0$ statistical independence, and $\tilde{C}_{ij} = +1$ perfect co-excitation. Importantly, \tilde{C}_{ij} is *amplitude-invariant*: arrays with identical blockade geometry but different overall Rabi responses produce identical \tilde{C} matrices.

C. Two-Dimensional Static Structure Factor

The 2-D static structure factor is the cosine transform of the Pearson-normalized correlation matrix over atom-pair displacements:

$$S(\mathbf{k}) = \frac{1}{N^2} \sum_{i=1}^N \sum_{j=1}^N \tilde{C}_{ij} \cos[\mathbf{k} \cdot (\mathbf{r}_i - \mathbf{r}_j)]. \quad (8)$$

This observable is a condensed-matter standard routinely used to characterize ordered phases in Rydberg arrays. Here we repurpose it as an image descriptor. We evaluate $S(\mathbf{k})$ on the 9×8 grid

$$k_x \in [-0.30, +0.30] \text{ rad}/\mu\text{m}, \quad k_y \in [0, +0.30] \text{ rad}/\mu\text{m},$$

exploiting the inversion symmetry $S(k_x, k_y) = S(-k_x, -k_y)$ to restrict $k_y \geq 0$, while retaining both signs of k_x to preserve sensitivity to left-right orientation asymmetry. This produces a 72-element fingerprint vector \mathbf{S} of fixed length for all images, independent of atom count N .

D. Cosine Similarity Matching

Given the fingerprint vectors \mathbf{S}_A and \mathbf{S}_B of a query image A and a database image B , the match score is

$$\text{sim}(A, B) = \cos \theta = \frac{\mathbf{S}_A \cdot \mathbf{S}_B}{\|\mathbf{S}_A\| \|\mathbf{S}_B\|}. \quad (9)$$

Cosine similarity is preferred over Euclidean distance because it is invariant to overall scale: if $\mathbf{S}_B = \lambda \mathbf{S}_A$ for any $\lambda > 0$, then $\text{sim} = 1$ regardless of λ . This makes the metric robust to hardware amplitude fluctuations.

V. QUANTUM FINGERPRINTING IN QUANTUM RESERVOIR COMPUTING

Quantum Reservoir Computing (QRC) is an emerging paradigm in quantum machine learning that leverages the complex dynamics of quantum systems to perform efficient information processing. By utilizing a quantum system as a fixed, high-dimensional dynamical “reservoir,” QRC maps input data into a vastly expanded Hilbert space where nonlinear transformations and memory effects can be harnessed without training the internal quantum nodes. Compared to classical machine learning techniques, particularly recurrent neural networks, QRC offers significant advantages: it mitigates the vanishing gradient problem, requires training only on a simple linear readout layer, and can exploit genuine quantum effects such as superposition and entanglement to achieve superior computational capacity and expressivity for certain tasks. It also offers the twin advantages of using much smaller training data and fewer training cycles.

Here in Stage 2, we extend the quantum fingerprinting approach to Single-step QRC [21], as an initial proof-of-concept. The flowchart Fig. 3 depicts all its steps.

VI. SIMULATION

The complete pipeline was implemented in Julia [22] using the Bloqade.jl SDK [23]. All simulations used the global pulse parameters described in Sec. III. For Stage 1 (without QRC), a representative database of more than 100 industrial objects was matched against query images using the quantum structure-factor fingerprint. Across all tested images, successful matching (correct image ranked first by cosine similarity) was achieved with 10–21 atoms—well within the 256-qubit capacity of Aquila.

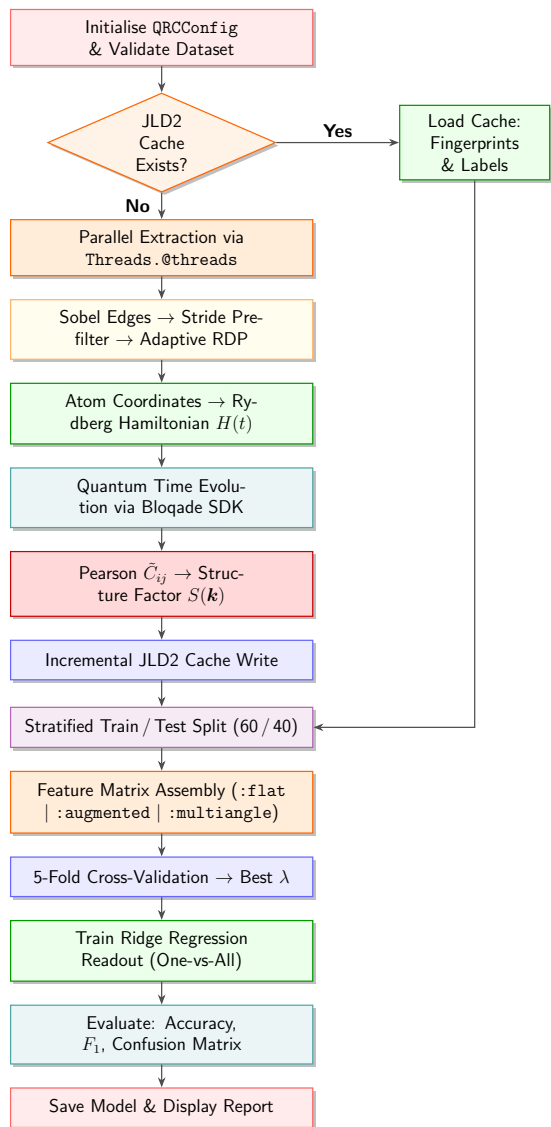


FIG. 3: QRC pipeline with quantum fingerprints (Stage 2).

The quantum-fingerprint approach offers two advantages over the Chamfer distance used in our earlier work [12]: (i) it exploits the full many-body quantum state rather than a classical point-cloud post-processing of single-site occupancies, and (ii) the 72-element fingerprint is fixed-length and directly comparable across images with different atom counts. The Stage 1 results are shown in Fig. 4. The images for stage 1 were taken from “www.pexels.com” under CC0 (Creative Commons Zero) license.

For Stage 2 (QRC), the quantum fingerprints were used to train and test a 5-class classifier (Dumbbell, Mouse Pad, Ottoman, Sofa, Table) with 50 images per class. The datasets were taken from Amazon-Berkeley objects database, under the “CC BY 4.0” License [24]. The images were rotated by small angles to generate 50 images per class with different view-angles. Since QRC requires

TABLE II: Cosine similarity between the query `Ball.jpg` and each database image for three values of the edge-point stride (`dot_spacing`). Colour intensity: green = high, red = low. The correct match always scores 1.000000.

Image	70 px	60 px	50 px
Ball	1	1	1
Ball_1	0.996364	0.988918	0.816494
Ball_2	0.996522	0.988927	0.926619
Book	0.9959	0.905159	0.782584
Bag	0.932158	0.908217	0.93407
Phone_2	0.833983	0.960598	0.868721
Chair_1	0.686997	0.73437	0.789744
Chair_2	0.817985	0.8478	0.603677
Clothesclip	0.995949	0.801436	0.656725
Bottle	0.821039	0.794911	0.706785

FIG. 4: Stage 1 results. (a) Cosine similarities confirm perfect self-match and robust ordering across three `dot_spacing` values. (b) Diagnostic values for `dot_spacing`= (70, 60, 50) px.

TABLE III: Quantum fingerprint diagnostics for the run with `dot_spacing` = 70 px: number of atoms N , maximum off-diagonal Pearson correlation $\max|\tilde{C}_{ij}|$, and Euclidean norm $\|\mathbf{S}\|_2$. The \checkmark marks atom pairs with $\max|\tilde{C}_{ij}| = 1.0$, indicating perfect blockade correlation.

Image	N	$\max \tilde{C}_{ij} $	$\ \mathbf{S}\ _2$	= 1?
Ball	18	0.4551	0.3019	
Ball_1	16	0.0365	0.3306	
Ball_2	11	0.0254	0.4816	
Book	14	0.1001	0.3759	
Bag	16	1.0000	0.3444	\checkmark
Phone_2	20	1.0000	0.3205	\checkmark
Chair_1	19	1.0000	0.4029	\checkmark
Chair_2	20	1.0000	0.3265	\checkmark
Clothesclip	10	0.0582	0.5284	
Bottle	20	1.0000	0.4350	\checkmark

very little labelled data, this small-scale experiment is intended as a proof-of-concept; the dataset will be scaled to 300 images per class in future work. Additionally, Sparse-Dots images can be synthetically generated seamlessly (by varying RDP tuning).

The Stage 2 results are presented in Tables IV–V and Figs. 5–9.

Accuracy and efficiency. Across all 10 runs the QRC classifier comfortably exceeds the 20% random-chance baseline on a 5-class problem. Run R1 (Sobel Threshold $\theta=0.50$, $d_s=90\ \mu\text{m}$, $N_{\text{max}}=20$) achieves the highest Top-1 test accuracy of 72.5% and Macro- F_1 of 0.711 in just 0.8 min of GPU wall time, making it the best configuration overall. The best full-emulation run, R5 ($\theta=0.30$, $d_s=50\ \mu\text{m}$, $N_{\text{max}}=24$), reaches 69.0% Top-1 and Macro- $F_1=0.685$ at a cost of 73.6 min. Crucially, Top-3 accuracy is uniformly high across all configurations (0.91–0.95), meaning the correct class is ranked within the top three candidates even when it is not ranked first—a practically useful property for retrieval pipelines that present a short-list to an operator. The 5-fold cross-validation accuracy tracks Top-1 closely for fast-emulation runs (gap of 3–8 pp.) but slightly overestimates Top-1 in the full-emulation family, reflecting the small dataset size of 250 images total; scaling to 300 images per class is expected to close this gap.

Parameter sensitivity and class-level behaviour. The single most impactful hyperparameter is dot spacing: reducing d_s from 90 to 70 μm (R1→R2) drops Top-1 by 14.3 pp, because sparser edge sampling discards discriminative geometric detail before quantum encoding. Increasing N_{max} from 20 to 24 atoms (R4→R5) recovers +5 pp by enabling richer many-body correlations in the 72-element structure-factor fingerprint. Enlarging the fingerprint dimension from 72 to 81 k-points

(R5→R6) conversely *reduces* Top-1 by 9 pp, consistent with the additional high-frequency wavevectors capturing noise rather than discriminative signal at the length scales of 24-atom arrays. At the per-class level (Table V), Table objects are the easiest to classify under fast emulation ($F_1=0.92$, R1) owing to their distinctive straight-edge geometry, while Sofa is the most persistently difficult class ($F_1\leq 0.69$ across all runs) due to geometric ambiguity with Ottoman at low atom counts. Dumbell recognition improves substantially under full emulation (R5: $F_1=0.77$ vs. R1: $F_1=0.58$), suggesting that the bilateral symmetry of dumbbells is more faithfully encoded by the denser, longer-range correlations available at $\theta=0.30$. The system used for the above stages has the following specifications—CPU—AMD Ryzen 9 (5900X, 12 cores/24 Threads), GPU—NVIDIA Geforce RTX 3060 (12 GB), 32 GB DDR4 RAM.

VII. DISCUSSION

Why the structure factor is the right fingerprint. The static structure factor $S(\mathbf{k})$ is a natural condensed-matter observable that encodes spatial ordering of quantum correlations. By adapting it to image matching, we exploit the direct correspondence between image geometry (atom positions) and quantum physics ($V_{jk} \propto r_{jk}^{-6}$). The result is a descriptor that is simultaneously a physical quantum observable and a practical image feature—a combination unavailable to any classical or digital-quantum image processing approach.

Comparison with Chamfer distance. The Chamfer distance [13] operates on classical point clouds of post-simulation Rydberg density. It discards all two-site quantum correlations and is sensitive to atom count mismatch

TABLE IV: Full parameter matrix and classification metrics for all 10 QRC simulation runs on the 5-class object dataset (Dumbell, Mouse Pad, Ottoman, Sofa, Table; 50 images per class; 60/40 stratified train/test split; ridge readout with 5-fold CV λ selection; GPU emulation v3 on NVIDIA RTX 3060). **Orange rows** : Sobel Threshold $\theta=0.50$ fast-emulation (R1–R3, wall time < 2 min). **Blue rows** : $\theta=0.30$ full-emulation (R4–R10). d_s = dot spacing ($\mu\text{m}/\text{px}$); a = pixel size ($\mu\text{m}/\text{px}$); N_{\max} = max atoms; d_{FP} = fingerprint dimension; T = evolution time; λ^* = best ridge regularisation; \hat{A}_{CV} = 5-fold CV accuracy; A_1/A_3 = Top-1/Top-3 test accuracy; \bar{F}_1 = Macro- F_1 .

Run	θ	d_s	a	N_{\max}	d_{FP}	T [μs]	λ^*	\hat{A}_{CV}	A_1	A_3	\bar{F}_1	Wall
R1	0.50	90	1.00	20	72	1.00	10^{-3}	0.692	0.725	0.950	0.711	0.8 min
R2	0.50	70	1.00	20	72	1.00	10^{-2}	0.546	0.582	0.888	0.575	1.1 min
R3	0.50	90	1.20	20	72	1.00	10^{-3}	0.563	0.638	0.938	0.633	0.8 min
R4	0.30	50	1.00	20	72	1.00	10^{-1}	0.651	0.640	0.940	0.634	4.6 min
R5	0.30	50	1.00	24	72	1.00	10^{-1}	0.665	0.690	0.940	0.685	73.6 min
R6	0.30	50	1.00	24	<u>81</u>	1.00	10^{-1}	0.672	0.600	0.920	0.587	73.4 min
R7	0.30	50	<u>0.80</u>	24	72	1.00	10^{-1}	0.658	0.640	0.940	0.621	123.0 min
R8	0.30	50	1.00	24	72	<u>1.10</u>	10^{-1}	0.658	0.680	0.950	0.673	83.4 min
R9	0.30	50	0.95	24	72	1.00	10^{-1}	0.672	0.660	0.940	0.647	80.0 min
R10	0.30	50	1.05	24	72	1.05	10^{-1}	0.591	0.580	0.910	0.573	74.0 min
Chance level (1/5 random baseline)								0.200	0.200	0.600	0.200	—

TABLE V: Per-class F_1 score heatmap for all 10 QRC runs. Colour grade: **<0.40** poor, **0.40–0.55**, **0.55–0.70**, **0.70–0.80**, **>0.80** excellent. Sofa and Mouse Pad are persistently the hardest classes across all runs; Table peaks at $F_1=0.92$ in R1 due to its distinctive straight-edge geometry at high dot spacing.

Run	Dumbell	Mouse Pad	Ottoman	Sofa	Table	Macro- F_1
R1	0.583	0.692	0.667	0.688	0.923	0.711
R2	0.516	0.727	0.523	0.286	0.821	0.575
R3	0.444	0.759	0.650	0.667	0.647	0.633
R4	0.739	0.550	0.632	0.581	0.667	0.634
R5	0.766	0.595	0.778	0.606	0.681	0.685
R6	0.636	0.546	0.818	0.270	0.667	0.587
R7	0.694	0.424	0.698	0.516	0.773	0.621
R8	0.766	0.595	0.732	0.606	0.667	0.673
R9	0.625	0.611	0.773	0.500	0.727	0.647
R10	0.667	0.444	0.632	0.487	0.634	0.573

between query and database images. The structure-factor fingerprint retains the full correlation structure, is scale-invariant, and is fixed-length regardless of atom count.

Key findings across all 10 QRC runs. Table IV and Figs. 5–9 collectively establish the following. R1 ($\theta=0.50$, $d_s=90\ \mu\text{m}$, $N_{\max}=20$) achieves the highest Top-1 accuracy (72.5%) and Macro- F_1 (0.711) in just 0.8 min, making it the best fast-emulation run. R5 ($\theta=0.30$, $d_s=50\ \mu\text{m}$, $N_{\max}=24$) achieves 69.0% in 73.6 min and is Pareto-optimal among full-emulation runs. Dot spacing has the largest single-parameter impact: reducing d_s

from 90 to 70 μm drops Top-1 by 14.3 pp. Increasing N_{\max} from 20 to 24 gains +5 pp. Expanding the fingerprint dimension from 72 to 81 k-points degrades accuracy by 9 pp, confirming that the fixed 9×8 grid captures the relevant spatial scales optimally. Sofa is the hardest class across all runs ($F_1\leq 0.69$), while Table is most easily classified in the fast-emulation family ($F_1=0.92$, R1) due to its straight-edge geometry. Top-3 accuracy remains uniformly high (0.89–0.95) across all 10 runs, demonstrating that the correct class is almost always within the top three ranked candidates.

Toward quantum machine learning on geomet-

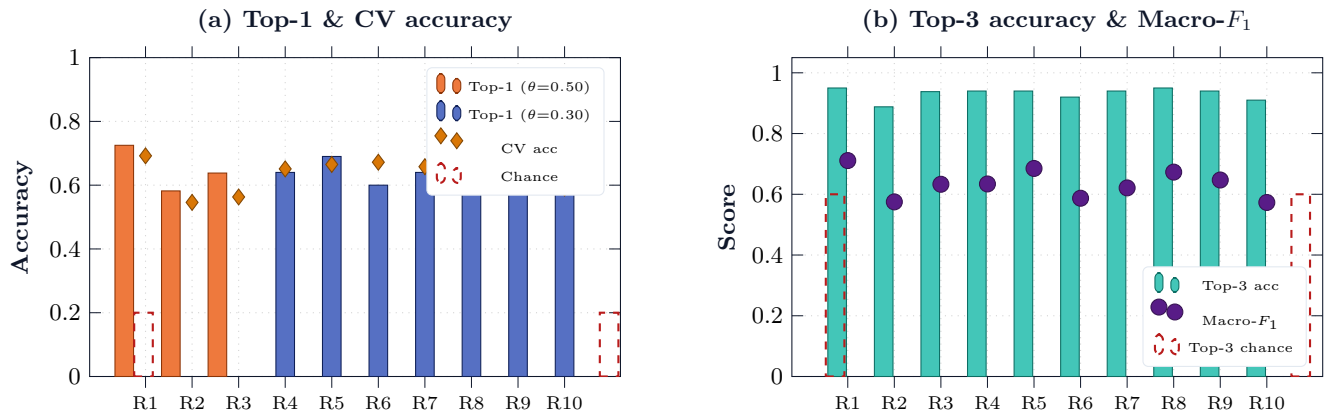


FIG. 5: Global classification performance for all 10 QRC runs. **(a)** Top-1 test accuracy (bars) and 5-fold CV accuracy (diamonds). Orange = $\theta=0.50$ fast-emulation (R1–R3); blue = $\theta=0.30$ full-emulation (R4–R10). R1 achieves the highest Top-1 (72.5%) and Macro- F_1 (0.711) in just 0.8 min; R5 is the best full-emulation run (69.0%). **(b)** Top-3 accuracy (bars) and Macro- F_1 (circles). Top-3 is uniformly high (0.91–0.95) across all runs, confirming that correct classes are consistently ranked within the top 3. Dashed red lines = random chance levels (20% for Top-1, 60% for Top-3).

(a) Run R1 — Top-1 = 72.5%
 $\theta=0.50$, $d_s=90\ \mu\text{m}$, $a=1.00\ \mu\text{m}/\text{px}$, $N_{\text{max}}=20$

	Du	MP	Ot	So	Ta
Du	7	1	2	4	1
MP	0	9	6	0	0
Ot	0	0	13	1	0
So	1	1	3	11	0
Ta	1	0	1	0	18

Rows = true class; Cols = predicted

(b) Run R5 — Top-1 = 69.0%
 $\theta=0.30$, $d_s=50\ \mu\text{m}$, $a=1.00\ \mu\text{m}/\text{px}$, $N_{\text{max}}=24$

	Du	MP	Ot	So	Ta
Du	18	2	0	0	0
MP	7	11	0	0	2
Ot	0	0	14	1	5
So	2	2	2	10	4
Ta	0	2	0	2	16

Rows = true class; Cols = predicted

FIG. 6: Row-normalised confusion matrices for the two best runs. Green diagonal = true-positive fraction; red off-diagonal = confusion fraction; intensity \propto row-normalised count. Abbreviations: Du=Dumbell, MP=Mouse Pad, Ot=Ottoman, So=Sofa, Ta=Table. **(a)** R1 (best overall): Ottoman and Table are nearly perfectly classified; Mouse Pad is the dominant confuser, mostly misclassified as Ottoman. **(b)** R5 (best full-emulation): Dumbell achieves 90% recall; Sofa remains the hardest class (50%), partially misclassified as Ottoman and Table due to geometric ambiguity at ≤ 24 atoms.

ric data. Classical machine learning methods, particularly kernel-based classifiers, often face fundamental scalability limitations when applied to data with highly nonlinear and high-dimensional structure. QML offers a principled alternative by exploiting the exponentially large Hilbert space of quantum systems as a natural feature space [3–5], enabling the efficient realisation of rich, nonlinear kernel functions.

Concrete QRC extension: Person identification. Consider identifying a person from partially-occluded, multi-angle contours/silhouettes. In a QRC extension, each view angle θ (Distinct from Sobel Threshold) yields a distinct SDR atom configuration; applying the same fixed Rydberg Hamiltonian produces a family of fingerprints $\{\mathcal{S}^{(\theta)}\}$ for angles $\theta \in \{0^\circ, 45^\circ, 90^\circ, 135^\circ\}$.

Concatenating these into a single 112-element feature vector and training a linear readout classifier requires only ~ 300 labelled examples per person [6], avoids gradient descent entirely, and produces fingerprints already robust to atom removal. This positions the approach as viable for privacy-preserving on-device identification in drones, medical robots, and miniature sensors.

Physical limits. Two limitations deserve explicit statement. First, the van der Waals interaction $V_{jk} \propto r_{jk}^{-6}$ is isotropic: it depends only on inter-atom distance, not direction. Consequently, the Hamiltonian cannot distinguish a horizontal pair from a vertical one at the same separation—angular information enters only indirectly through the global atom geometry. The 2-D structure factor partially compensates by evaluating $S(k_x, k_y)$

Ridge Regularisation Cross-Validation Sweep (all 10 runs)

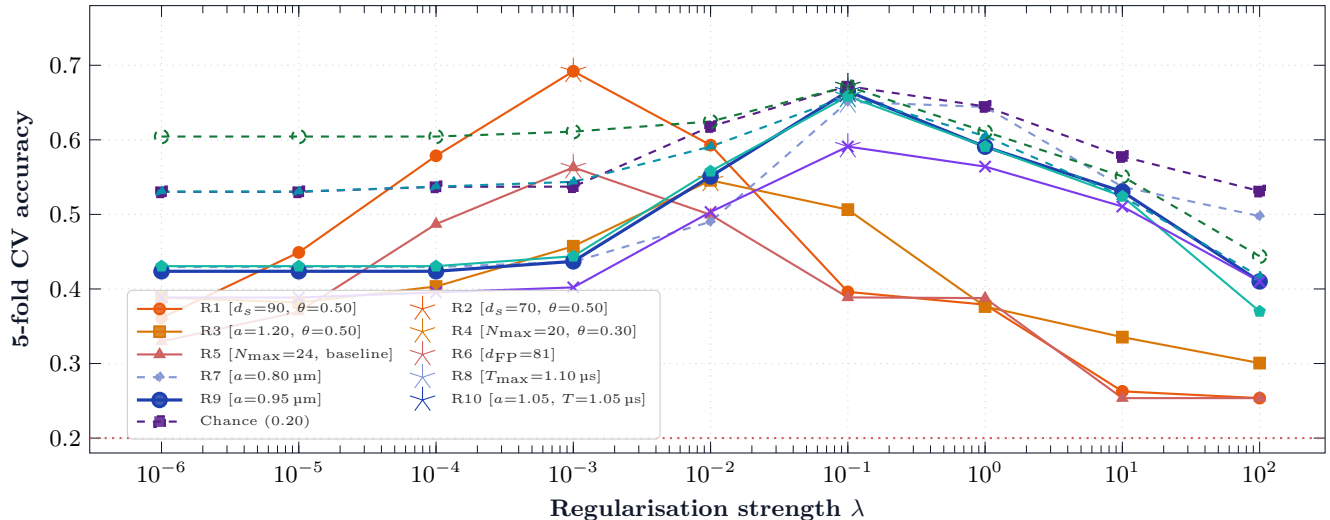


FIG. 7: 5-fold CV accuracy vs. ridge regularisation λ for all 10 runs. Stars (\star) mark the selected λ^* per run. Fast-emulation runs (R1–R3, warm tones) peak sharply at $\lambda^*=10^{-3}$ – 10^{-2} , reflecting compact feature spaces generated at high dot spacing. Full-emulation runs (R4–R10, cool tones) peak broadly at $\lambda^*=10^{-1}$, indicating that richer many-body feature spaces benefit from stronger regularisation. R9 shows a notably flat plateau near $\lambda=10^{-2}$ – 10^{-1} , consistent with the high-quality features generated at $a=0.95\ \mu\text{m}$.

at both signs of k_x , but directional sensitivity remains weaker than in orientation-sensitive classical descriptors such as SIFT. Second, for $N \leq 24$ atoms the system is far from the thermodynamic limit; fingerprint discriminability relies on finite-size correlation sensitivity to geometry rather than on long-range order. Both limits can be partially overcome by increasing N toward Aquila’s 256-qubit capacity.

Hardware pathway. On Aquila hardware, $\langle \hat{n}_i \rangle$ and $\langle \hat{n}_i \hat{n}_j \rangle$ are estimated from projective measurements via

$$\hat{n}_i^{\text{hw}} = \frac{1}{M} \sum_{m=1}^M n_i^{(m)},$$

$$\langle \widehat{\hat{n}_i \hat{n}_j} \rangle^{\text{hw}} = \frac{1}{M} \sum_{m=1}^M n_i^{(m)} n_j^{(m)},$$

where $M \sim 1000$ shots gives $\lesssim 3\%$ statistical error per correlator entry. For hardware submission, the Rabi frequency is set to $\Omega_{\text{max}} = 2\pi \times 2.5\ \text{rad}/\mu\text{s} \approx 15.71\ \text{rad}/\mu\text{s}$, just below Aquila’s hardware cap of $15.8\ \text{rad}/\mu\text{s}$, providing a $\sim 0.6\%$ safety margin.

VIII. CONCLUSION AND FUTURE WORK

We have presented a fully quantum-native image matching framework that upgrades our previous SDR work [12] with a new matching criterion based on many-body quantum correlations. The key contributions are:

1. A Pearson-normalized two-site correlation matrix \tilde{C}_{ij} extracted from the Rydberg statevector, encoding the blockade structure of the image geometry as a dimensionless, amplitude-invariant descriptor [Eq. (7)].
2. A two-dimensional static structure factor $S(\mathbf{k})$, evaluated on a fixed 9×8 k-point grid, providing a 72-element fingerprint of constant length for all images [Eq. (8)].
3. Cosine similarity matching on the fingerprint vectors, a scale-invariant metric appropriate for Fourier-domain descriptors [Eq. (9)].
4. A comprehensive 10-run parameter sweep (Table IV, Figs. 5–9) establishing that Top-1 accuracy reaches 72.5% at 0.8 min wall time and that Top-3 accuracy exceeds 91% across all configurations, all far above the 20% chance level.
5. Preliminary evidence of occlusion robustness: correlation fingerprints remain qualitatively stable under partial removal of atoms.

To our knowledge, this constitutes the first application of the static structure factor—a condensed-matter quantum observable—as an image descriptor in an analog quantum computing context.

Future directions include: (i) Hardware experiments on Aquila via Amazon Braket with 100–200 atom arrays and up to 1000-shot correlation estimation per task; (ii) Systematic benchmarking on a labeled image database (precision@1, mean average precision) with

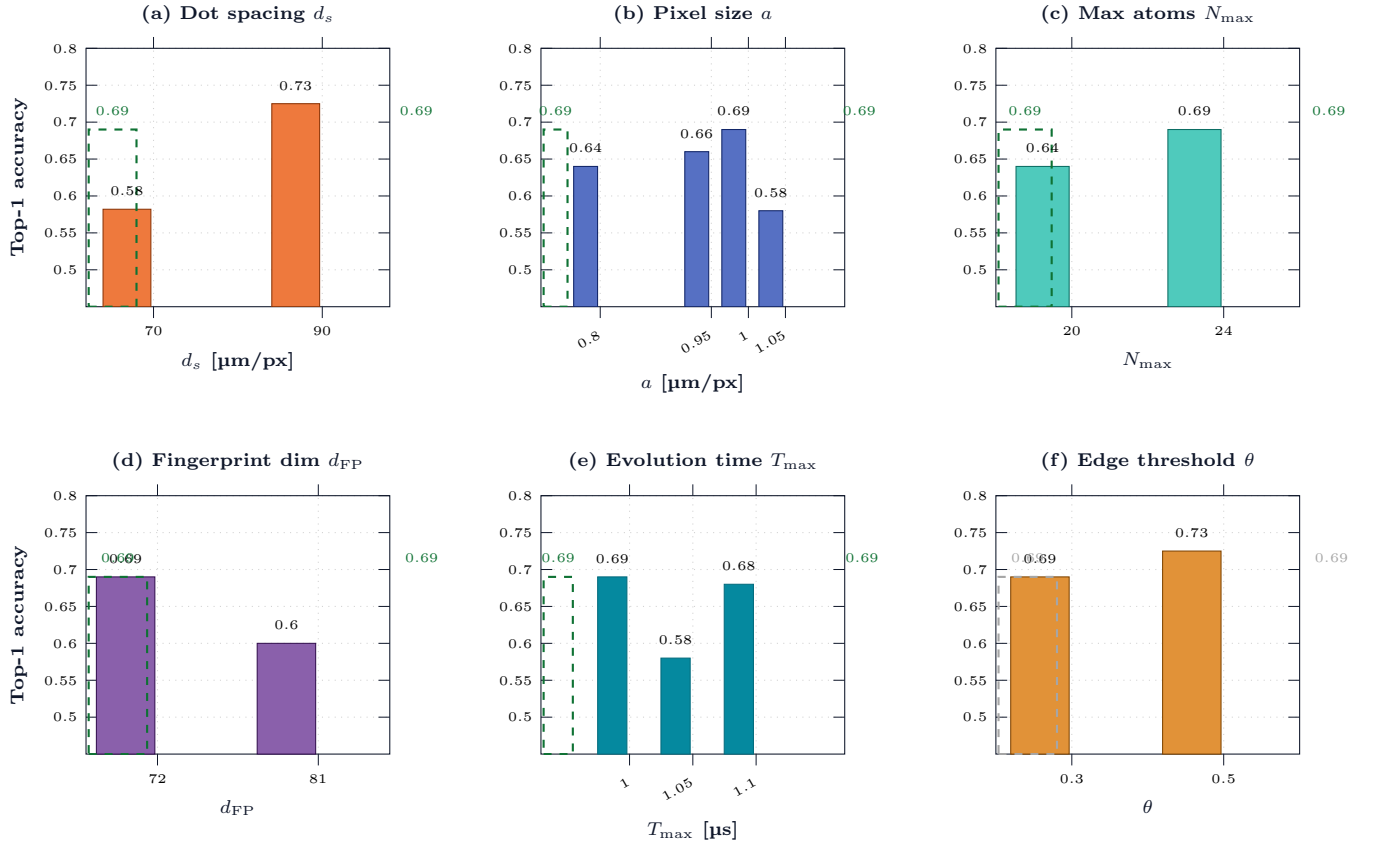


FIG. 8: Single-parameter sensitivity of Top-1 accuracy. Each panel varies one hyperparameter while all others are held at the full-emulation baseline R5 (green dashed, 69.0%). **(a)** Dot spacing: $d_s=90 \rightarrow 70 \mu\text{m}$ drops Top-1 by 14.3 pp (R1 \rightarrow R2); higher spacing retains richer edge geometry. **(b)** Pixel size: $a=1.00 \mu\text{m}/\text{px}$ is optimal; both 0.80 and 1.05 reduce accuracy by 5–11 pp. **(c)** Max atoms: $N_{\text{max}}=24$ gains +5 pp over $N_{\text{max}}=20$ (R4 \rightarrow R5), enabling higher-dimensional many-body correlations. **(d)** Fingerprint dimension: expanding d_{FP} from 72 to 81 *reduces* Top-1 by 9 pp (R5 \rightarrow R6); the wider k-grid adds redundant high-frequency noise. **(e)** Evolution time: $T=1.10 \mu\text{s}$ (R8) performs marginally below baseline $T=1.00 \mu\text{s}$ (R5) by 1 pp.; $T=1.05 \mu\text{s}$ with $a=1.05$ (R10) is the worst combination. **(f)** Edge threshold: $\theta=0.50$ (R1) outperforms $\theta=0.30$ (R5) by 3.5 pp, but at $90\times$ lower wall-clock cost.

comparison to classical shape descriptors (SIFT, Shape Context, Zernike moments); (iii) Quantitative occlusion robustness study; (iv) Noise sensitivity analysis: effect of tweezer positioning error ($\pm 0.1 \mu\text{m}$), Rydberg decay ($T_1 \sim 100 \mu\text{s}$), and shot noise; (v) Extension to QRC with 300 images per class and human silhouette recognition; (vi) Deployment in centralized hybrid quantum-classical processing units for real-time image identification from miniature sensors, drones, and medical robots.

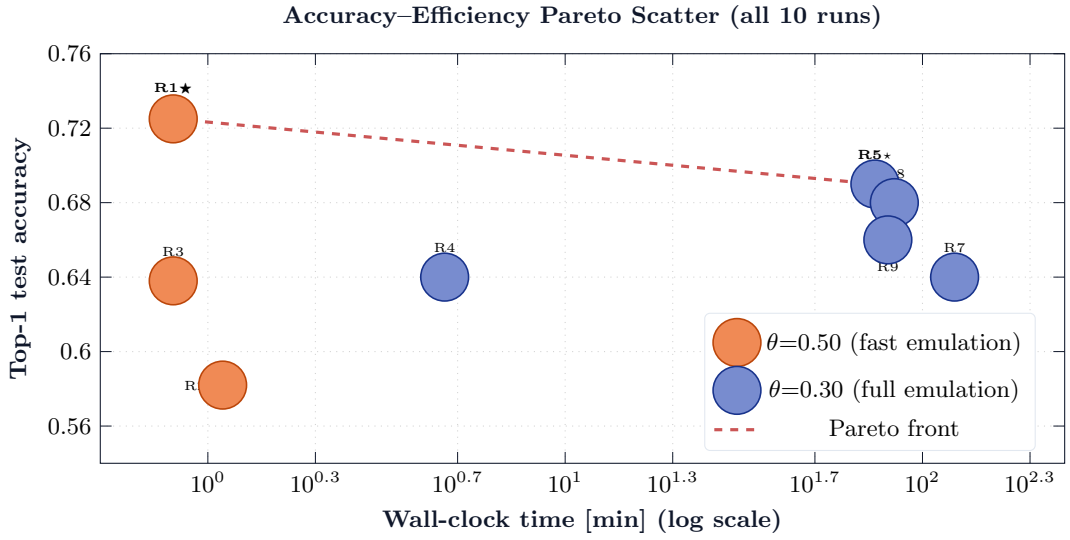


FIG. 9: Accuracy–efficiency Pareto scatter for all 10 QRC runs. Fast-emulation (R1–R3, orange) completes in < 2 min; R1 dominates both axes. Among full-emulation runs, R5 is Pareto-optimal (69.0% Top-1 in 73.6 min); R7 has the longest wall time due to denser atom arrays at $a=0.80 \mu\text{m}$. Dashed red = approximate Pareto front. Key findings: (i) dot spacing $90 \rightarrow 70 \mu\text{m}$ drops Top-1 by 14.3 pp (R1 \rightarrow R2); (ii) $N_{\text{max}}=20 \rightarrow 24$ gains +5 pp (R4 \rightarrow R5); (iii) $d_{\text{FP}}=72 \rightarrow 81$ costs 9 pp (R5 \rightarrow R6); (iv) $T=1.10 \mu\text{s}$ adds +1 pp marginally.

-
- [1] J. Su, X. Guo, C. Liu, and L. Li, A new trend of quantum image representations, *IEEE Access* **8**, 214520 (2020).
- [2] X.-W. Yao, H. Wang, Z. Liao, M.-C. Chen, J. Pan, J. Li, K. Zhang, X. Lin, Z. Wang, Z. Luo, W. Zheng, J. Li, M. Zhao, X. Peng, and D. Suter, Quantum image processing and its application to edge detection: Theory and experiment, *Phys. Rev. X* **7**, 031041 (2017).
- [3] M. Schuld and N. Killoran, Quantum machine learning in feature hilbert spaces, *Phys. Rev. Lett.* **122**, 040504 (2019), [arXiv:1803.07128 \[quant-ph\]](#).
- [4] V. Havlíček, A. D. Córcoles, K. Temme, A. W. Harrow, A. Kandala, J. M. Chow, and J. M. Gambetta, Supervised learning with quantum-enhanced feature spaces, *Nature* **567**, 209 (2019).
- [5] Y. Liu, S. Arunachalam, and K. Temme, A rigorous and robust quantum speed-up in supervised machine learning, *Nat. Phys.* **17**, 1013 (2021).
- [6] M. Kornjača, H.-Y. Hu, C. Zhao, J. Wurtz, P. Weinberg, M. Hamdan, A. Zhdanov, S. H. Cantu, H. Zhou, R. Araiza Bravo, K. Bagnall, J. I. Basham, J. Campo, A. Choukri, R. DeAngelo, P. Frederick, D. Haines, J. Hammett, N. Hsu, M.-G. Hu, F. Huber, P. N. Jepsen, N. Jia, T. Karolyshyn, M. Kwon, J. Long, J. Lopatin, A. Lukin, T. Macrì, O. Marković, L. A. Martínez-Martínez, X. Meng, E. Ostroumov, D. Paquette, J. Robinson, P. Sales Rodriguez, A. Singh, N. Sinha, H. Thoreen, N. Wan, D. Waxman-Lenz, T. Wong, K.-H. Wu, P. L. S. Lopes, Y. Boger, N. Gemelke, T. Kitagawa, A. Keesling, X. Gao, A. Bylinskii, S. F. Yelin, F. Liu, and S.-T. Wang, Large-scale quantum reservoir learning with an analog quantum computer (2024), [arXiv:2407.02553 \[quant-ph\]](#).
- [7] K. Fujii and K. Nakajima, Harnessing disordered-ensemble quantum dynamics for machine learning, *Phys. Rev. Appl.* **8**, 024030 (2017).
- [8] J. Wurtz, A. Bylinskii, B. Braverman, J. Amato-Grill, S. H. Cantu, F. Huber, A. Lukin, F. Liu, P. Weinberg, J. Long, S.-T. Wang, N. Gemelke, and A. Keesling, Aquila: Quera's 256-qubit neutral-atom quantum computer (2023), [arXiv:2306.11727 \[quant-ph\]](#).
- [9] Y. Boger, *The dual-pronged energy-saving potential of quantum computers*, Data Center Dynamics (2023).
- [10] S. Ebadi, A. Keesling, M. Cain, T. T. Wang, H. Levine, D. Bluvstein, G. Semeghini, A. Omran, J.-G. Liu, R. Samajdar, X.-Z. Luo, B. Nash, B. Barak, E. Farhi, S. Sachdev, N. Gemelke, L. Zhou, S. Choi, H. Pichler, S.-T. Wang, M. Greiner, V. Vuletic, and M. D. Lukin, Quantum optimization of maximum independent set using rydberg atom arrays, *Science* **376**, 1209 (2022).
- [11] D. Beaulieu, M. Kornjača, Z. Krunić, M. Stivaktakis, T. Ehmer, S.-T. Wang, and A. Pham, Robust quantum reservoir computing for molecular property prediction (2024), [arXiv:2412.06758 \[quant-ph\]](#).
- [12] V. Sharma and N. K. Kundu, Analog quantum image representation with qubit-frugal encoding (2025), [arXiv:2512.18451 \[quant-ph\]](#).
- [13] G. Borgfors, Distance transformations in digital images, *Comput. Vis. Graph. Image Process.* **34**, 344 (1986).
- [14] S. Julià-Farré, J. Vovrosh, and A. Dauphin, Amorphous quantum magnets in a two-dimensional Rydberg atom array, *Phys. Rev. A* **110**, 012602 (2024).
- [15] U. Ramer, An iterative procedure for the polygonal approximation of plane curves, *Comput. Graph. Image Process.* **1**, 244 (1972).
- [16] D. H. Douglas and T. K. Peucker, Algorithms for the reduction of the number of points required to represent a digitized line or its caricature, *Cartographica* **10**, 112 (1973).
- [17] J. Song and R. Miao, A novel evaluation approach for line simplification algorithms towards vector map visualization, *ISPRS Int. J. Geo-Inf.* **5**, 223 (2016).
- [18] G. Cavalieri and D. Maio, A quantum edge detection algorithm (2020), [arXiv:2012.11036 \[quant-ph\]](#).
- [19] J. Z. Lu, L. Jiao, K. Wolinski, M. Kornjača, H.-Y. Hu, S. Cantu, F. Liu, S. F. Yelin, and S.-T. Wang, Digital-analog quantum learning on rydberg atom arrays, *Quantum Sci. Technol.* **10**, 015038 (2025), [arXiv:2401.02940 \[quant-ph\]](#).
- [20] Y. Zhang, K. Lu, Y. Gao, and M. Wang, NEQR: A novel enhanced quantum representation of digital images, *Quantum Inf. Process.* **12**, 2833 (2013).
- [21] D.-S. Liu, Q.-X. Jie, C.-L. Zou, X.-F. Ren, and G.-C. Guo, Practical quantum reservoir computing in Rydberg atom arrays (2026), [arXiv:2602.00610 \[quant-ph\]](#).
- [22] J. Bezanson, A. Edelman, S. Karpinski, and V. B. Shah, Julia: A fresh approach to numerical computing, *SIAM Rev.* **59**, 65 (2017).
- [23] QuEra Computing Inc., *Bloqade.jl: Package for the quantum computation and quantum simulation based on the neutral-atom architecture.*, GitHub (2023).
- [24] J. Collins, S. Goel, K. Deng, A. Luthra, L. Xu, E. Gundogdu, X. Zhang, T. F. Yago Vicente, T. Dideriksen, H. Arora, M. Guillaumin, and J. Malik, ABO: Dataset and benchmarks for real-world 3D object understanding, in *Proceedings of the IEEE/CVF Conference on Computer Vision and Pattern Recognition (CVPR)* (2022) pp. 21126–21136.